Ahmed Allam[1]
School of Mechanical Engineering,
Georgia Institute of Technology,
Atlanta, GA 30332
e-mail: a.allam@gatech.edu

Christopher Sugino
School of Mechanical Engineering,
Georgia Institute of Technology,
Atlanta, GA 30332
e-mail: csugino@gatech.edu

Matthew Harding
Tronosjet Manufacturing,
Charlottetown, PE C1C 1N2, Canada
e-mail: mharding@tronosjet.com

D. Paul Bishop
Department of Mechanical Engineering,
Dalhousie University,
Halifax, NS B3H 4R2, Canada
e-mail: paul.bishop@dal.ca

Alper Erturk
School of Mechanical Engineering,
Georgia Institute of Technology,
Atlanta, GA 30332
e-mail: alper.erturk@me.gatech.edu

Massimo Ruzzene
Department of Mechanical Engineering,
University of Colorado Boulder,
Boulder, CO 80309
e-mail: massimo.ruzzene@colorado.edu

Phased Array Ultrasonic Testing of Inconel 625 Produced by Selective Laser Melting

We investigate the use of phased array ultrasonic testing (PAUT) as an offsite non-destructive quality assurance technique for parts made by selective laser melting (SLM). SLM is a popular additive manufacturing (AM) approach for fabricating high-value metallic components with complex geometries. Slight variations in the laser power during fabrication might lead to internal defect development within the part, which could compromise its mechanical strength and fatigue life. PAUT is employed to detect typical internal porosity generated in Inconel 625 samples due to laser power fluctuation during SLM. The typical defect size, shape, and distribution are first identified using metallography and X-ray computed tomography (XCT). B-Scan images of the defect region is then generated experimentally using a 5-MHz linear UT phased array probe. Finite elements simulate wave propagation using geometries obtained from XCT images. The simulation results are compared to the experimental imaging of large defect regions and then used to generate total focusing method images of isolated clusters of 50–200 μm defects. The testing technique illustrates a successful application of PAUT for quality inspection of SLM parts.
[DOI: 10.1115/1.4050963]

Keywords: ultrasonic imaging, additive manufacturing, finite element analysis, lack of fusion defects, product quality control

1 Introduction

Additive manufacturing (AM) is an enabling technology that has been quickly moving from rapid prototyping to production of complex, high-value, low-volume components. Selective laser melting (SLM) is a powder bed fusion (PBF) AM technique that involves melting powdered material deposited layer by layer on a printing bed [1,2]. It is gaining traction for its ability to generate parts of complex geometry with minimal post-processing [3]. In SLM, a laser power source is used to supply the necessary energy to convert selective regions of the powder material to a melt pool which solidifies to form the desired part geometry. The rest of the powder is left to act as a support for subsequent layers. However, producing a high-quality SLM part is contingent on delivering the right amount of energy to melt the powder [4,5]. If the deposited energy deviates from its optimum value, different types of defects can form within the manufactured part. A slight variation of the process parameters while manufacturing might lead to the formation of microscale defects and porosity that affect the reliability of the part. Both the fatigue life [6,7] and the mechanical strength [8,9] of the AM part could be compromised by the presence of any porosity [10]. Moreover, due to the layer-by-layer building associated with SLM and AM in general, defects that are hard to detect without the use of NDT techniques [11] may arise during printing.

Several techniques are used to detect defects in AM parts. Infrared thermography [12–15] and eddy current testing (ECT) [16,17] have been used for in situ detection of defects and for controlling the printing process. Others are more oriented toward inspecting the completed part. For example, microscopy techniques, such as optical microscopy [4,18] and scanning electron microscopy (SEM) [5,6,19], were traditionally used to inspect the microstructure of AM parts. While SEM can achieve sub-micron image resolution, it cannot image internal defects without the destruction of the sample (i.e., sectioning and polishing). Recently, X-ray computed tomography (XCT) has become the standard method for visualizing internal defects and porosity in additively manufactured components through the generation of high-resolution volumetric images [7,20–23]. XCT is useful for accurately studying the internal structure of the part; however, it is expensive when used for ongoing quality control purposes and requires elevated safety precautions. Additionally, thick parts made of heavy metal alloys such as Inconel are challenging to inspect using XCT, since they strongly attenuate X-rays.

Multiple ultrasonic testing (UT) approaches have been used to inspect PBF manufactured parts [24]. Ultrasonic wave velocity and attenuation measured using pulse-echo techniques have been used to estimate the overall porosity [25] and residual stresses [26] in AM parts and to calculate their elastic constants [27,28]. Traditional UT transducers fitted below the build of a 3D printer were used to detect delamination and loss of power while printing [29,30]. Immersion pulse-echo techniques were also used to detect internal defects using a single probe [31] and linear and annular phased arrays [32]. Laser-induced ultrasonic (LIU) surface waves (Rayleigh waves) have also been suggested for the in situ detection of near-surface defects as the part is being printed [33–35]. This approach proposes the use of two lasers other than the main laser source used to manufacture the part: a source laser excites ultrasonic surface waves near the surface of the sample, and a second continuous wave laser with an interferometer measures the surface velocity of the sample.

However, experimental demonstrations of this technique in SLM have been limited to ex situ AM samples, due to the complexity of integrating it to the build chamber and the noise generated by the main (high power) laser [36]. More recent efforts have suggested using LIU to generate and measure the propagation of bulk shear waves for the inspection of the internal defects in AM parts [37–39]. In these efforts, the full matrix capture (FMC) method [40] was used to acquire point response from different linear locations of the sample to emulate a phased array, then internal sectorial images of a 3D printed block were constructed using the total focusing method (TFM) [41].

In this work, we investigate the feasibility of using phased array ultrasonic testing (PAUT) to detect internal defects generated during SLM. The nature, size, and distribution of the expected defects were first identified by deliberately varying the laser power at predefined regions in the AM samples, then imaging their internal cross sections using optical metallography and XCT techniques. Then, a linear PAUT probe imaged the samples using traditional linear scanning. The finite element method (FEM) simulated the propagation of elastic waves in the AM samples and their interaction with the generated defects. The defect geometry was obtained from XCT images, and traditional B-scan as well as the TFM post-processing algorithms were implemented to image defects from simulation data. The effect of the flaw size, location, distribution, and material properties on the constructed image and the detectability of defects were then outlined from FEM simulation results.

2 Fabrication of the Test Samples

A Renishaw RenAM 500Q system was used to fabricate test samples with deliberate defects. For this commercial system, the energy density incident on the powder bed by the laser (ED) can be approximated by

$$ED = \frac{P \cdot E}{HS \cdot PD \cdot t} \qquad (1)$$

where P is the laser power, E is the exposure time, HS is the hatch spacing, PD is the point distance, and t is the layer thickness. It should be noted that this equation may look slightly different compared to the typical equation used for SLM [19] where scan speed is incorporated. The system utilized operates with a modulated laser (compared to the more common continuous lasers), where the energy density is controlled by laser exposure time and point distance as opposed to laser scan speed in common systems. The value of the energy density has a strong effect on the quality of the AM part. Low energy density is often associated with lack of fusion defects, while high energy density leads to key-holing (gas porosity) defects [4,6]. While all the parameters in Eq. (1), as well as other parameters such as various powder aspects, have different effects on the quality of the generated part, the total energy density is the most important factor when it comes to the formation of internal porosity [6,11]. Thus, by only varying the laser power about the optimal operating conditions during printing, typical (practical) defects could be generated in the sample.

Three identical sets of cylindrical samples were manufactured to be inspected using a different approach. Each set contained six cylinders made of Inconel 625 alloy with different printing conditions as summarized in Table 1 and Fig. 1. Each sample was divided into two regions to emulate the fluctuation of the laser from optimal conditions. For all samples, the shell region (see Fig. 1) was printed using the power recommended by the manufacturer (Renishaw) for printing Inconel 625 (200 W). The effect of incident energy density fluctuation during the printing process was studied by varying the laser power only at the core region, where each sample was set to have a different value from 100 W to 300 W as summarized in Table 1. The remaining 3D printing parameters were kept constant and are summarized in Table 2.

All samples were printed simultaneously, and visual inspection of the samples during the printing process revealed a different

Table 1 Summary of the laser power used at the core region of the 3D printed samples

Sample #	Laser power (core region) [W]	Energy density [J/mm^3]
1	200[a]	74.1
2	100	37.0
3	150	55.6
4	200	74.1
5	250	92.6
6	300	111.1

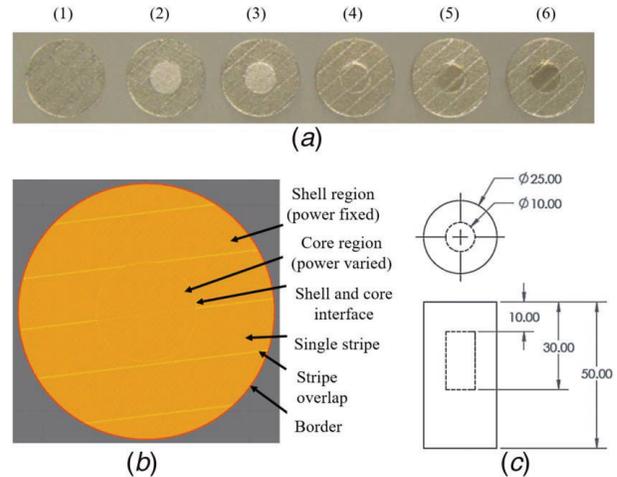[a]Printed without the shell and core regions distinction.

Fig. 1 (a) Top view of the SLM samples taken during their 3D printing. The laser power used at the core region is summarized in Table 1. Note that Sample 1 was printed without the shell and core regions distinction. (b) Different regions as defined during the 3D printing of the SLM samples. (c) Schematic showing the geometry of the samples and the dimensions of the internal defect region (dimensions are in millimeters).

Table 2 3D printing process parameters used in the fabrication of the samples

Parameter	Unit	Value
Layer thickness	μm	30
Point distance	μm	70
Exposure time	μs	70
Hatch spacing	μm	90
Stripe size	mm	5
Stripe offset	mm	0.1

visual appearance between the core regions as shown in Fig. 1(a). The first set of samples was investigated destructively by sectioning and polishing each sample and investigating the internal structure by optical microscopy as discussed in Sec. 3. The second set was imaged using XCT as discussed in Sec. 4, and the third set was reserved for preliminary PAUT inspection (Sec. 5).

3 Metallography Inspection

A single sample set (1–6) was sectioned, mounted, and polished in both the $x - y$ (build plane) orientation, along with the $x - z$ (build direction) orientation. Standard polishing steps for Inconel 625 were utilized, progressing from 220 grit to 0.05 μm colloidal silica. Since the main goal was limited to defect identification, etching was not undertaken. Imaging was undertaken using a
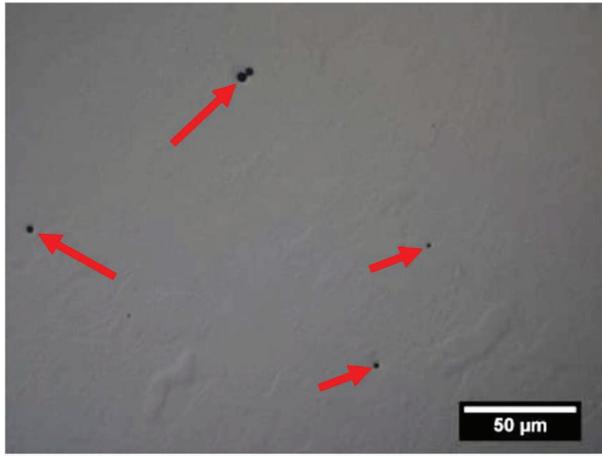
Fig. 2 Representative image showing porosity within samples printed with the OEM recommended setting of 200 W laser power

Zeiss optical microscope with magnification ranging from 50× to 500×. Samples and regions printed with the original equipment manufacturer (OEM) recommended settings (200 W laser power), including the "shell" region of all samples, along with core regions of samples 1 and 4, showed a highly dense material, with sporadic, isolated, and mainly highly spherical pores of sizes typically ranging from sub-micron to a few microns in size (shown in Fig. 2, with pores indicated by arrows). Only Sample 2 (100 W laser power) showed variation in porosity/defects within the core region (Fig. 3) when compared to the OEM recommended setting of 200 W (as shown in Fig. 2). These defects within the 100 W sample core (Fig. 3(a)) are distinctly caused by lack of fusion, with a highly irregular morphology and clear evidence of un-melted powder particles, a result of the reduced energy density incident on the powder bed. Defects of sizes up to 200 μm were detected.

No definitive evidence of a higher degree of defects arising from laser power in the range of 150–300 W within the core region was identified, alluding to quite a high range of suitable power settings within the process to ensure good fusion. It should be noted that our approach only considered a single key process variable, and when combined with variations in other parameters affecting the melt-solidification process (e.g., hatch spacing, point distance, exposure time, etc.), it would likely change. Also, this investigation was not extensive, and variations within the microstructure or other aspects may affect the overall performance of the built material, limiting this operating window.

The only other sample/location where a definitive variation in porosity was seen was at the interface of the shell and core regions within Sample 6 (300 W laser power), as shown in Fig. 4. A clear trend of highly spherical pores with a size up to 50 μm can be seen along the interface region. Due to the size and morphology of these pores, along with the higher laser power setting, the pore generation is likely a result of the key-holing effect, resulting in trapped gas porosity within the built material. It is unclear why these defects only occurred at the interface region and not within the core section as a whole.

4 X-Ray Computed Tomography Inspection

Since Sample 2 revealed the highest defect density from optical inspection, the nature of the defects was further investigated by imaging the internal structure of the sample using XCT. Several aspects represented a challenge for XCT scanning. Inconel is a dense nickel alloy with relatively large attenuation for X-rays. Moreover, the large sample size prohibited getting the fine resolution necessary to resolve expected defects, as XCT image resolution depends on the scanning volume. To overcome these limitations and facilitate the acquisition of high resolution XCT images, the sample was machined down to 15 mm diameter, and only a length of 12 mm was scanned as a representative volume of the internal defect structure of the sample. XCT images were obtained for Sample 2 through the commercial services of North Star Imaging Inc. Two internal cross sections of the generated 3D image are shown in Fig. 5. The images were generated with a resolution (voxel size) of 4.5 μm, which was enough to identify defects down to 10 μm. The XCT results show a uniform distribution of
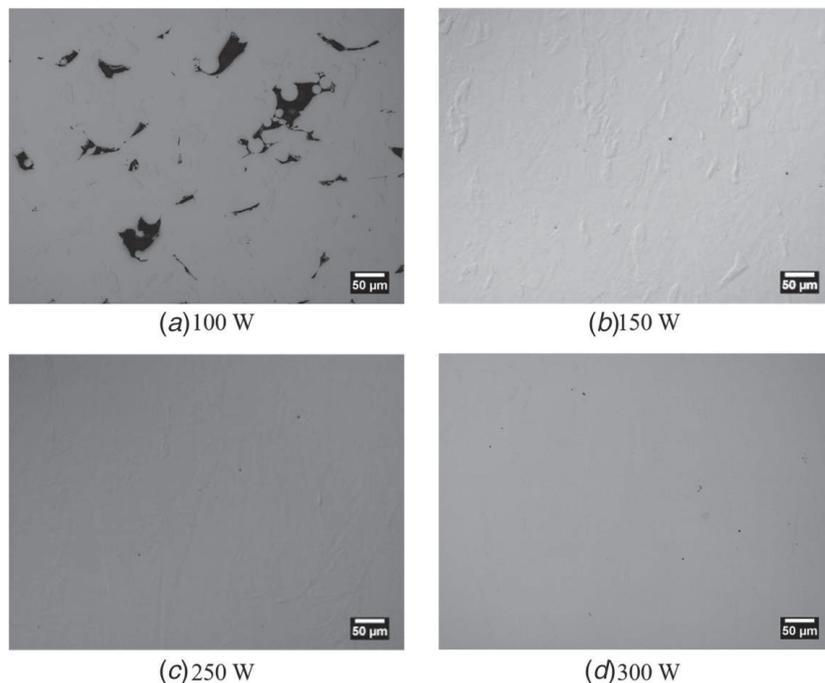

Fig. 3 Core region optical images of Samples: (a) 2–100 W, (b) 3–150 W, (c) 5–250 W, and (d) 6–300 W

Fig. 4 Interface of shell and core regions within Sample 6. Note the mark at the bottom center of the image was added to indicate the location of the interface region and is not part of the microstructure.

defects in the core region caused by lack of fusion due to the insufficient laser power, and the defect size determined from the XCT results agrees with the optical observations.

5 Ultrasonic Phased Array Testing

A preliminary ultrasonic inspection was performed on the sample with the largest defect density (Sample 2). A Doppler Phascan

phased array system with 64/16 receiver/pulser channels acquired linear B-scan images using a 64-element linear phased array probe. The 5L64-0.6x10 FBA312 probe had a center frequency of 5 MHz, a pitch of 0.6 mm, and an elevation of 10 mm. The probe was mounted on a rexolite flat wedge of thickness 20 mm and longitudinal wave speed of 2337 m/s. The cylindrical sample was scanned from the top flat surface as shown in Fig. 6(a). The system was programmed to perform a linear scan with an aperture of eight elements and a step of one element without focusing. The depth information in the B-scan image was calculated using the longitudinal wave speed of homogeneous Inconel 625 (5711 m/s). The resulting B-scan image is shown in Fig. 6(b) with the expected defect region shown in dashed lines. The top interface region appears clearly in the image and agrees well with the projected location of the defect. The bottom interface of the defect shows in the image as well; however, it is lower than the projected location of the defect region. Moreover, the defect region appears as a scattering domain with multiple weaker signals generated from the inhomogeneity of the region. Since the defect size ranges from 10 μm to 150 μm, which is much smaller than the longitudinal wavelength in Inconel at 5 MHz ($\lambda = 1.1$ mm), the individual defects generate multiple scattered wavefields which were captured in the image, and the main ultrasonic pulse travels with a lower wave speed in the defect region compared to the defect-free region. This lower wave speed explains why the lower interface appears below the expected location of the defect region in Fig. 6(b).

6 Finite Element Model for Ultrasonic Wave Propagation

A two-dimensional (2D) linear elastic FEM model for simulating the propagation of ultrasonic waves in the 3D printed sample was
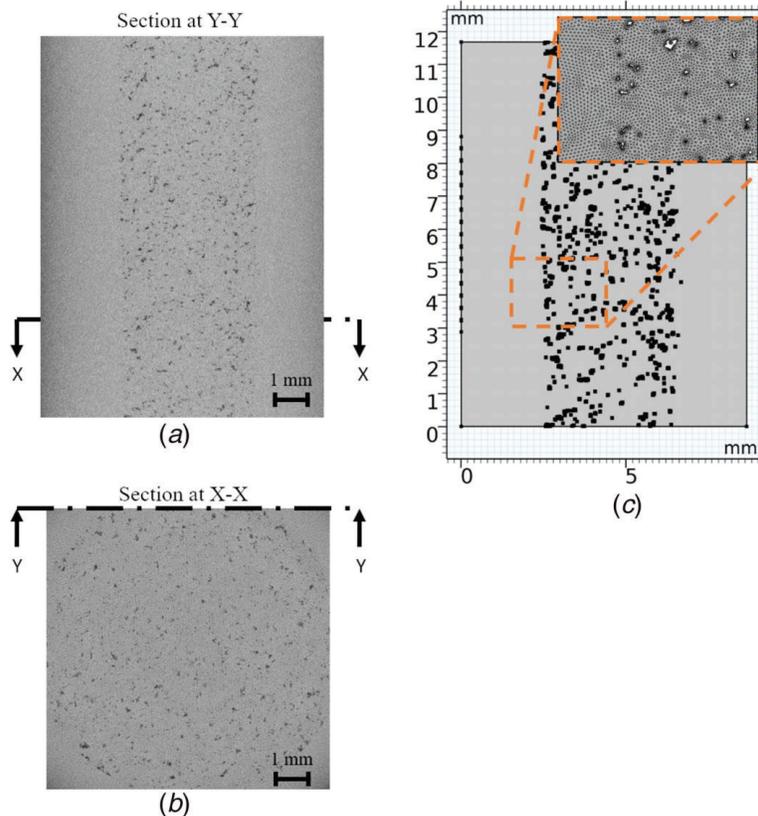

Fig. 5 (a) Front and (b) top cross sections of an X-ray CT scan of Sample 2 showing a uniform distribution of the defects in the core region. (c) Defect geometry as generated from the XCT images to be used in FEM wave propagation simulations.
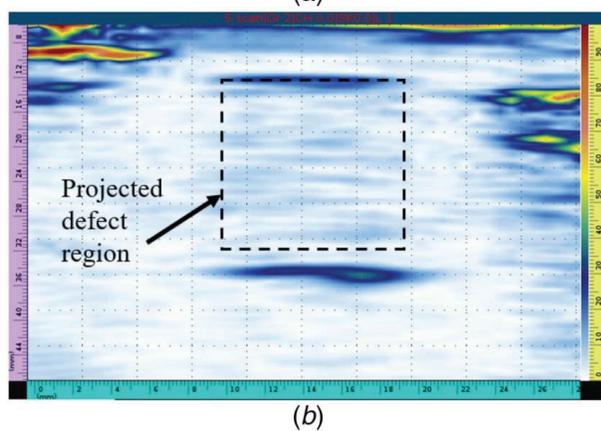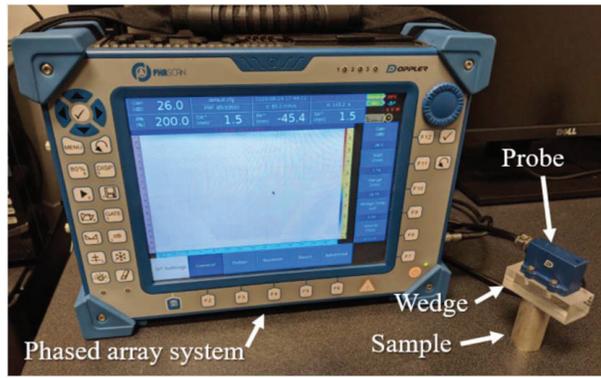
Fig. 6 Experimental setup for imaging the internal structure of the samples using a 5-MHz 64 element array set for a linear B-scan. The image for Sample 1 is shown on the screen in (a) and that for Sample 2 is shown in (b) with the projected defect region highlighted.

constructed using COMSOL MULTIPHYSICS® commercial software [42]. The XCT image shown in Fig. 5(a) was used to generate 2D geometry to be used in ultrasonic wave propagation simulations. To generate the defect geometry, the XCT image was first smoothed using a 2D averaging filter to remove high frequency CT noise. The resulting image was then segmented into a binary image of the background and defect regions by setting an intensity threshold. The final defect geometry was generated by converting the binary image into a DXF CAD file using the trace bitmap tool in INKSCAPE open source software.

The defects were modeled as free internal boundary conditions in a homogeneous domain with the elastic material properties of Inconel 625 ($E = 205$ GPa, $\rho = 8250$ kg/m^3, and $\nu = 0.29$). The homogeneous domain was discretized with triangular elements smaller than $\lambda/5$, where λ is the smallest wavelength in Inconel 625 (shear wavelength). The ultrasonic phased array probe was modeled as an array of line segments on the top edge of the domain as shown in Fig. 7. To simulate an excitation pulse on a segment, a normal external force was applied with a Gaussian pulse time series defined by

$$F_i(t) = \frac{1}{\sqrt{2\pi}\sigma} \sin(2\pi f_o t) e^{-(t-(1/W))^2/2\sigma^2} \qquad (2)$$

$$\sigma = \frac{\sqrt{\ln(2)}}{\pi W} \qquad (3)$$

where $F_i(t)$ is the applied force on element i, f_o is the center frequency of the array in Hz, and W is the 3 dB bandwidth of the array. The response of each element in the time domain was recorded by averaging the normal velocity over the length of the element. The response of the array was simulated by exciting each element i and recording the response of all elements to construct the full matrix of the array (R). This approach is commonly known as the FMC [40]. The element of the full matrix of the array is given by $R_{ij}(t)$ which is the envelope of the time response
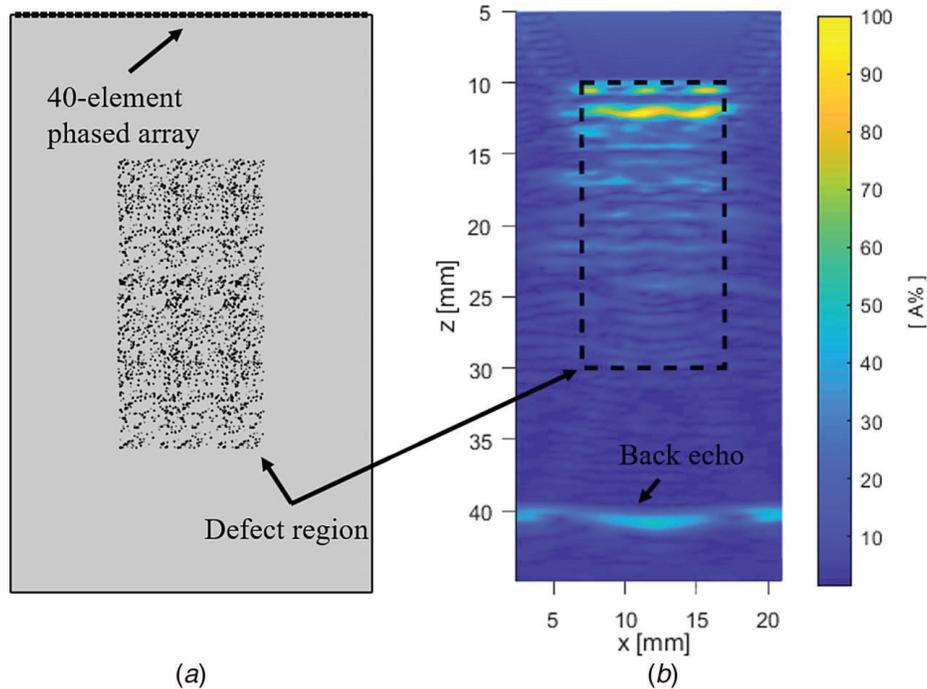

Fig. 7 (a) Constructed geometry for visualizing the wave propagation through Sample 2. The defect geometry was extracted from XCT images. (b) Linear B-scan image of the sample generated by a 40-element array with an aperture of eight elements.
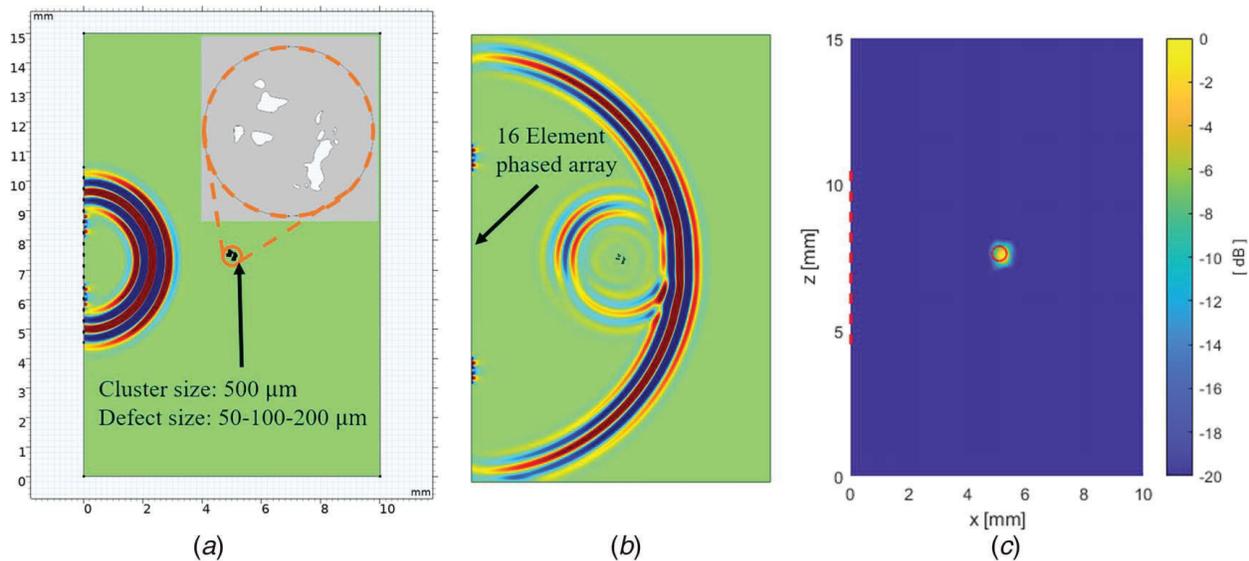
Fig. 8 (a and b) Two time snapshots showing the propagation and reflection of longitudinal waves generated by a single phased array element and reflected from a cluster of defects of size 500 μm located at 5 mm depth. (c) The TFM image as constructed from the FMC data of the phased array shown in (b). The cluster of defects location is highlighted with a circle.

measured at element j when element i is excited with a Gaussian pulse. The full matrix R can then be used to construct the array image using different post-processing algorithms.

6.1 Interface Detection Using B-Scan. The traditional B-scan image (linear scan) is constructed from the FMC data by summing the full matrix elements according to the relation [41]:

$$I(x_k, z) = \sum_{i=k}^{k+S} \sum_{j=k}^{k+S} R_{ij}\left(\frac{2z}{c_p}\right) \qquad (4)$$

where $I(x, z)$ is the B-scan image, $x_k = k\, P + S/2$, $k \in \{1, N-S\}$ is the scan line location where P is the array pitch, z is the depth, N is the number of elements in the array, S is the number of elements in the aperture, and c_p is the longitudinal wave speed in Inconel. A simulated B-scan image of Sample 2 (Fig. 7(b)) was generated by repeating the porosity geometry obtained from the XCT sample to fill the entire core region. This was done since the obtained XCT volumetric image was only a part of the actual core region. The image was generated using 40 array elements with an aperture of eight elements. The resulting image shows the top surface of the core region as well as the multiple instances of scattering inside it, similar to what was observed experimentally in Fig. 6(b). However, the simulated image failed to capture the bottom reflection of the core region captured in the experiments. This was attributed to the 2D nature of the FEM simulations, as the geometry was assumed to extend indefinitely in the out of plane direction. Since the porosity has a geometry of spherical nature, the 2D model tends to overestimate its effect and thus the results deviate from the experimental measurements. One solution for this would be to use full 3D wave propagation simulations; however, this would increase the number of degrees-of-freedom significantly.

6.2 Detection of Clusters of Isolated Defects Using Total Focusing Method. In a normal 3D printing process, the variation of the laser power is expected to be minimal. Clusters of smaller defects as shown in Fig. 8(a) are more likely to occur than continuous large domains of defects. To assess the applicability of using PAUT to detect practical defects in SLM, an isolated cluster of defects was simulated separately to assess their detectability. A
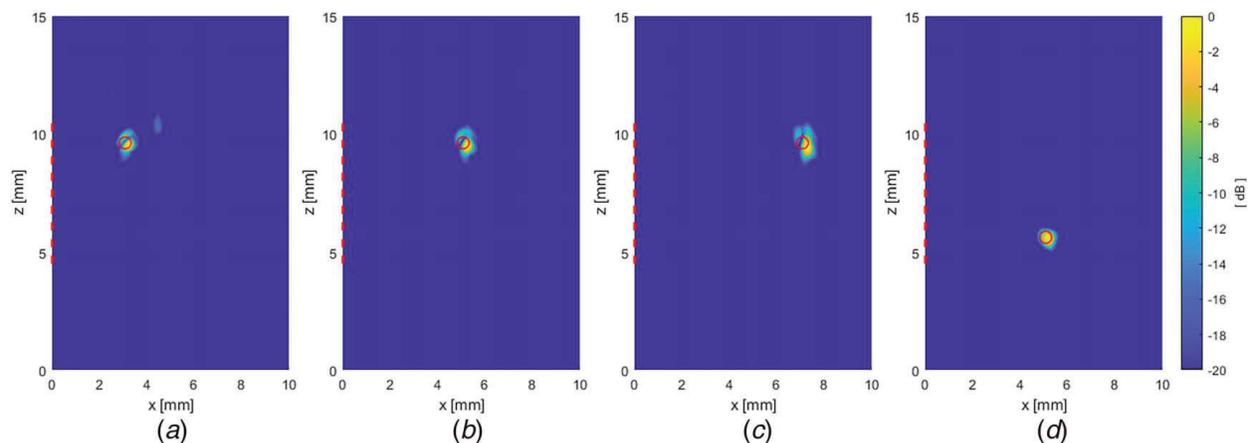

Fig. 9 TFM images generated for clusters of defects located at +2 mm from the center of the array and a depth of (a) 3 mm, (b) 5 mm, and (c) 7 mm. A cluster at −2 mm and a depth of 5 mm is shown in (d). In all cases, the defect cluster location is highlighted with a circle, and the phased array location is highlighted with a dashed line.
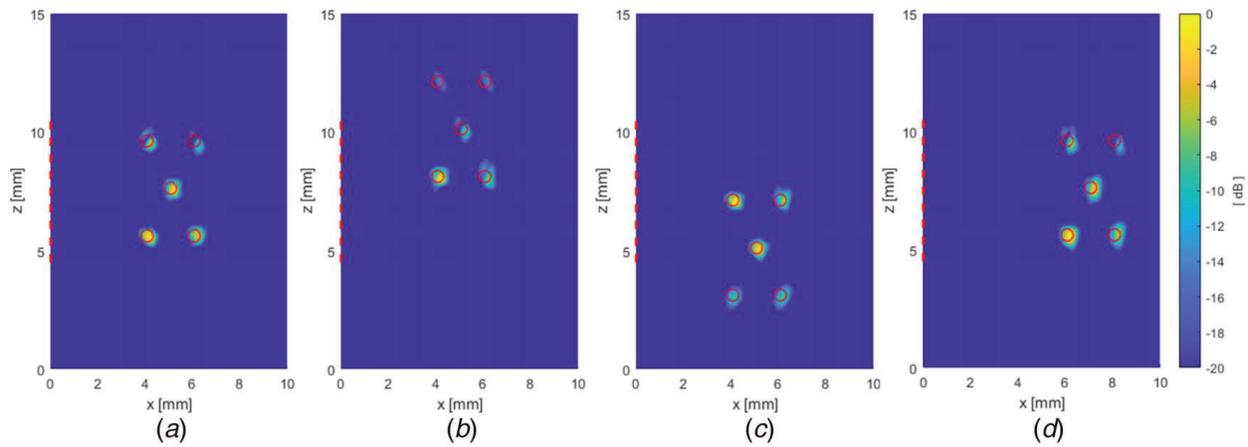
Fig. 10 TFM images generated for multiple clusters of defects present in the same sample. The locations of the defect clusters are highlighted with circles, and the phased array location is highlighted with a dashed line. The probe is centered about the defects in (a), shifted by −2.5 mm in the z-direction in (b) and by +2.5 mm in (c). The depth of the defects is shifted by 2.5 mm in the x-direction in (d).

cluster of diameter 500 μm was isolated from the XCT image which included individual defect dimensions with feature lengths of 50, 100, and 200 μm. A 16-element phased array with a center frequency of 10 MHz and a pitch of 370 μm was used to image the cluster of defects. The defect cluster was placed at a depth of 5 mm and the FMC of the array was simulated using the procedure described in Sec. 6. Figures 8(a) and 8(b) show two time snapshots of the propagation and reflection of ultrasonic waves as they are excited from a central element of the array. Because of the irregular geometry of the defects and their distribution in the cluster, the reflected (scattered) waves are not symmetric which might affect the generated UT image depending on the location of the array with respect to the defect.

UT images were generated from the FMC data using the TFM, since it is known to generate more focused images compared to traditional linear B-scan images [40]. The TFM image is calculated using the relation:

$$I(x, z) = \left| \sum_{i=1}^{N} \sum_{j=1}^{N} \tilde{R}_{ij} \left(\frac{\sqrt{(x_i - x)^2 + (z_i - z)^2}}{c_p} \right. \right.$$
$$\left. \left. + \frac{\sqrt{(x_j - x)^2 + (z_j - z)^2}}{c_p} \right) \right| \quad (5)$$

where $\tilde{R}_{ij}(t)$ is in-phase/quadrature signal obtained by applying the complex Hilbert transform to the element signal.

The generated TFM image is shown in Fig. 8(c) along with the expected defect cluster location. The signal is displayed in a logarithmic scale and the color range is clipped between −20 and 0 dB where 0 dB represents the maximum normalized signal. The defect cluster is clearly visible in the image; however, the individual defects were not resolved since they are smaller than the wavelength of the incident waves. The defect image is asymmetric which is mainly due to the irregular shape of the defects in the cluster.

The effect of having the defect at different locations with respect to the array is shown in Fig. 9. The defect cluster was placed at a ±2 mm offset from the center of the array and the depth was varied from 3 mm to 7 mm. Due to the irregular shape of the defect cluster, its image changed as its location with respect to the array changed. In Figs. 9(a)–9(c), the cluster image shows two distinguishable regions which reflect the geometry of the defect cluster shown in Fig. 8(a). This distinction is not visible when the cluster is on the other side of the array as shown in Fig. 9(d). This was attributed to the asymmetry of the reflected waves from the defect cluster due to its shape as shown in Fig. 8(b). The image of the defect was further distorted as its

depth location increased in Figs. 9(a)–9(c). This was attributed to the diminished active aperture of the array as the defect is located farther from the excited surface. A shadow appears when the defect is close to the array, as shown in Fig. 9(a), which is caused by multiple reflections from the cluster of defects and the generation of shear waves in addition to the pressure waves used in the imaging algorithm. However, this shadow is not visible when the array is located farther as shown in Figs. 9(b)–9(d).

6.3 Detection of Multiple Clusters of Defects. The effect of having multiple defect clusters was investigated in Fig. 10. Five defect clusters, with the same geometry shown in Fig. 8(a), were considered, and their location was changed to investigate its effect on the generated image. In all the considered cases, the signal from the defects placed below the centerline of the array was stronger and the defects appeared brighter than those placed above it. Even though the defects' size is too small to be resolved by ultrasonic waves at 10 MHz, their geometry and distribution had a strong effect on their image as detected by the array. However, all the defect clusters were detected for each considered case. In Fig. 10(a), defects at the top were resolved to two distinct regions, while defects at the center and the bottom were detected as a single region. When all the defects were shifted upwards as shown in Fig. 10(a), the top defects (furthest from the center of the array) were barely visible compared to the other defects. However, when all the defects were shifted downwards as shown in Fig. 10(c), the bottom defects (furthest from the center of the array) were still clearly visible. This suggests that the location of the defect cluster and its geometry both have a strong influence on the generated TFM image. The defects were shifted away from the transducer in Fig. 10(d) and the brightness of the top right defect is again lower than the other defects due to a combination of its position and orientation with respect to the array.

7 Conclusions

Phased array ultrasonic testing was investigated as an approach to detect lack of fusion defects typically generated due to loss of power during selective laser melting of Inconel 625. Typical defects were generated in cylindrical samples by varying the laser power during printing. The size of the defects was then identified using metallurgy and X-ray computed tomography techniques and was found to range between 5 and 200 μm. The defect distribution was uniform in volumes of the sample where the laser power dropped. Ultrasonic phased arrays captured lack of fusion defect regions, even though the defect size is smaller than the typical wavelength

of longitudinal ultrasonic waves. High-fidelity 2D UT simulations were conducted to evaluate the feasibility of using ultrasonic phased arrays to capture clusters of lack of fusion defects with a feature length smaller than 200 μm, and the results suggest that ultrasonic imaging is effective at detecting these class of defects. Results show that high-fidelity 2D simulations tend to overestimate the reflected signals from sub-wavelength defects. Simulations also show that the image of a cluster of subwavelength defects will depend on the geometry and distribution of the defects as well as their location with respect to the array.

Future work to this study includes experimental TFM imaging of isolated clusters of defects generated in a 3D-printed part to determine the minimum detectable defect size. It also includes studying defects generated in complex geometries and their detectability using ultrasonic phased arrays.

Conflict of Interest

There are no conflicts of interest.

References

[1] Rombouts, M., Kruth, J. P., Froyen, L., and Mercelis, P., 2006, "Fundamentals of Selective Laser Melting of Alloyed Steel Powders," CIRP. Ann., **55**(1), pp. 187–192.

[2] Yap, C. Y., Chua, C. K., Dong, Z. L., Liu, Z. H., Zhang, D. Q., Loh, L. E., and Sing, S. L., 2015, "Review of Selective Laser Melting: Materials and Applications," Appl. Phys. Rev., **2**(4), p. 041101.

[3] Thijs, L., Verhaeghe, F., Craeghs, T., Humbeeck, J. V., and Kruth, J.-P., 2010, "A Study of the Microstructural Evolution During Selective Laser Melting of Ti–6Al–4V," Acta. Mater., **58**(9), pp. 3303–3312.

[4] Ng, G. K. L., Jarfors, A. E. W., Bi, G., and Zheng, H. Y., 2009, "Porosity Formation and Gas Bubble Retention in Laser Metal Deposition," Appl. Phys. A, **97**(3), p. 641.

[5] Gong, H., Rafi, K., Gu, H., Starr, T., and Stucker, B., 2014, "Analysis of Defect Generation in Ti–6Al–4V Parts Made Using Powder Bed Fusion Additive Manufacturing Processes," Addit. Manuf., **1–4**, pp. 87–98.

[6] Liu, Q. C., Elambasseril, J., Sun, S. J., Leary, M., Brandt, M., and Sharp, P. K., 2014, "The Effect of Manufacturing Defects on the Fatigue Behaviour of Ti-6Al-4V Specimens Fabricated Using Selective Laser Melting," Adv. Mater. Res., **891–892**, pp. 1519–1524.

[7] Siddique, S., Imran, M., Rauer, M., Kaloudis, M., Wycisk, E., Emmelmann, C., and Walther, F., 2015, "Computed Tomography for Characterization of Fatigue Performance of Selective Laser Melted Parts," Mater. Des., **83**, pp. 661–669.

[8] Olakanmi, E. O., Cochrane, R. F., and Dalgarno, K. W., 2015, "A Review on Selective Laser Sintering/Melting (SLS/SLM) of Aluminium Alloy Powders: Processing, Microstructure, and Properties," Prog. Mater. Sci., **74**, pp. 401–477.

[9] Salarian, M., Asgari, H., and Vlasea, M., 2020, "Pore Space Characteristics and Corresponding Effect on Tensile Properties of Inconel 625 Fabricated Via Laser Powder Bed Fusion," Mater. Sci. Eng. A., **769**, p. 138525.

[10] Gong, H., Rafi, K., Gu, H., Janaki Ram, G. D., Starr, T., and Stucker, B., 2015, "Influence of Defects on Mechanical Properties of Ti–6Al–4V Components Produced by Selective Laser Melting and Electron Beam Melting," Mater. Des., **86**, pp. 545–554.

[11] Taheri, H., Shoaib, M. R. B. M., Koester, L. W., Bigelow, T. A., Collins, P. C., and Bond, L. J., 2017, "Powder-based Additive Manufacturing – a Review of Types of Defects, Generation Mechanisms, Detection, Property Evaluation and Metrology," Int. J. Additive Subtractive Mater. Manufact., **1**(2), pp. 172–209.

[12] Krauss, H., Eschey, C., and Zaeh, M. F., 2012, "Thermography for Monitoring the Selective Laser Melting Process," Solid Freeform Fabrication Symposium, Austin, TX, University of Texas at Austin, pp. 999–1014.

[13] Moylan, S., Whitenton, E., Lane, B., and Slotwinski, J., 2014, "Infrared Thermography for Laser-based Powder Bed Fusion Additive Manufacturing Processes," AIP. Conf. Proc., **1581**(1), pp. 1191–1196.

[14] Farshidianfar, M. H., Khajepour, A., and Gerlich, A., 2016, "Real-time Control of Microstructure in Laser Additive Manufacturing," Int. J. Adv. Manuf. Technol., **82**(5), pp. 1173–1186.

[15] Farshidianfar, M. H., Khajepour, A., and Gerlich, A. P., 2016, "Effect of Real-Time Cooling Rate on Microstructure in Laser Additive Manufacturing," J. Mater. Process. Technol., **231**, pp. 468–478.

[16] Todorov, E., Boulware, P., and Gaah, K., 2018, "Demonstration of Array Eddy Current Technology for Real-time Monitoring of Laser Powder Bed Fusion Additive Manufacturing Process," Nondestructive Characterization and Monitoring of Advanced Materials, Aerospace, Civil Infrastructure, and Transportation XII, Denver, CO, Vol. 10599, International Society for Optics and Photonics, p. 1059913.

[17] Kobayashi, N., Yamamoto, S., Sugawara, A., Nakane, M., Tsuji, D., Hino, T., Terada, T., and Ochiai, M., 2019, "Fundamental Experiments of Eddy Current Testing for Additive Manufacturing Metallic Material Toward In-Process Inspection," AIP. Conf. Proc., **2102**(1), p. 070003.

[18] Bauereiß, A., Scharowsky, T., and Körner, C., 2014, "Defect Generation and Propagation Mechanism During Additive Manufacturing by Selective Beam Melting," J. Mater. Process. Technol., **214**(11), pp. 2522–2528.

[19] Vandenbroucke, B., and Kruth, J.-P., 2007, "Selective Laser Melting of Biocompatible Metals for Rapid Manufacturing of Medical Parts," Rapid. Prototyp. J., **13**(4), pp. 196–203.

[20] Leuders, S., Thöne, M., Riemer, A., Niendorf, T., Tröster, T., Richard, H. A., and Maier, H. J., 2013, "On the Mechanical Behaviour of Titanium Alloy TiAl6V4 Manufactured by Selective Laser Melting: Fatigue Resistance and Crack Growth Performance," Int. J. Fatigue., **48**, pp. 300–307.

[21] du Plessis, A., Els, J., Booysen, G., and Blaine, D. C., 2015, "Application of MicroCT to the Non-destructive Testing of An Additive Manufactured Titanium Component," Case Stud. Nondestructive Testing Eval., **4**, pp. 1–7.

[22] Kim, F. H., Villarraga-Gomez, H., and Moylan, S. P., 2016, "Inspection of Embedded Internal Features in Additively Manufactured Metal Parts Using Metrological X-ray Computed Tomography," ASPE/euspen 2016 Summer Topical Meeting: Dimensional Accuracy and Surface Finish in Additive Manufacturing, Raleigh, NC, American Society for Precision Engineering, ASPE, Vol. 64, p. 6.

[23] Zhou, X., Dai, N., Chu, M., Wang, L., Li, D., Zhou, L., and Cheng, X., 2020, "X-ray CT Analysis of the Influence of Process on Defect in Ti-6Al-4V Parts Produced with Selective Laser Melting Technology," Int. J. Adv. Manuf. Technol., **106**(1), pp. 3–14.

[24] Honarvar, F., and Varvani-Farahani, A., 2020, "A Review of Ultrasonic Testing Applications in Additive Manufacturing: Defect Evaluation, Material Characterization, and Process Control," Ultrasonics, **108**, p. 106227.

[25] Karthik, N., Gu, H., Pal, D., Starr, T., and Stucker, B., 2013, "High Frequency Ultrasonic Non Destructive Evaluation of Additively Manufactured Components," 24th International SFF Symposium – An Additive Manufacturing Conference, SFF 2013, Austin, TX, University of Texas at Austin, pp. 311–325.

[26] Sealy, M. P., Hadidi, H., Sotelo, L. D., Li, W. L., Turner, J. A., and McGeough, J. A., 2020, "Compressive Behavior of 420 Stainless Steel After Asynchronous Laser Processing," CIRP. Ann., **69**(1), pp. 169–172.

[27] Foster, D. R., Dapino, M. J., and Babu, S. S., 2013, "Elastic Constants of Ultrasonic Additive Manufactured Al 3003-H18," Ultrasonics, **53**(1), pp. 211–218.

[28] Javidrad, H. R., and Salemi, S., 2020, "Determination of Elastic Constants of Additive Manufactured Inconel 625 Specimens Using An Ultrasonic Technique," Int. J. Adv. Manuf. Technol., **107**(11), pp. 4597–4607.

[29] Rieder, H., Spies, M., Bamberg, J., and Henkel, B., 2016, "On- and Offline Ultrasonic Characterization of Components Built by SLM Additive Manufacturing," AIP. Conf. Proc., **1706**(1), p. 130002.

[30] Nadimpalli, V. K., Yang, L., and Nagy, P. B., 2018, "In-situ Interfacial Quality Assessment of Ultrasonic Additive Manufacturing Components Using Ultrasonic NDE," NDT & E International, **93**, pp. 117–130.

[31] Song, Y., Zi, X., Fu, Y., Li, X., Chen, C., and Zhou, K., 2018, "Nondestructive Testing of Additively Manufactured Material Based on Ultrasonic Scattering Measurement," Measurement, **118**, pp. 105–112.

[32] Li, W., Zhou, Z., and Li, Y., 2019, "Application of Ultrasonic Array Method for the Inspection of TC18 Addictive Manufacturing Titanium Alloy," Sensors, **19**(20), p. 4371.

[33] Cerniglia, D., Scafidi, M., Pantano, A., and Rudlin, J., 2015, "Inspection of Additive-manufactured Layered Components," Ultrasonics, **62**, pp. 292–298.

[34] Davis, G., Nagarajah, R., Palanisamy, S., Rashid, R. A. R., Rajagopal, P., and Balasubramaniam, K., 2019, "Laser Ultrasonic Inspection of Additive Manufactured Components," Int. J. Adv. Manuf. Technol., **102**(5), pp. 2571–2579.

[35] Chen, D., Lv, G., Guo, S., Zuo, R., Liu, Y., Zhang, K., Su, Z., and Feng, W., 2020, "Subsurface Defect Detection Using Phase Evolution of Line Laser-generated Rayleigh Waves," Optics Laser Technol., **131**, p. 106410.

[36] Everton, S. K., Hirsch, M., Stravroulakis, P., Leach, R. K., and Clare, A. T., 2016, "Review of in-situ Process Monitoring and in-situ Metrology for Metal Additive Manufacturing," Mater. Des., **95**, pp. 431–445.

[37] Stratoudaki, T., Clark, M., and Wilcox, P. D., 2016, "Laser Induced Ultrasonic Phased Array Using Full Matrix Capture Data Acquisition and Total Focusing Method," Opt. Express, OE, **24**(19), pp. 21921–21938.

[38] Stratoudaki, T., Javadi, Y., Kerr, W., Wilcox, P. D., Pieris, D., and Clark, M., 2018, "Laser Induced Phased Arrays for Remote Ultrasonic Imaging of Additive Manufactured Components," 57th Annual Conference of the British Institute of Non-Destructive Testing, NDT 2018, Nottingham, UK, British Institute of Non-Destructive Testing, pp. 174–182.

[39] Pieris, D., Stratoudaki, T., Clare, A., Lukacs, P., Smith, R. J., Wilcox, P., and Clark, M., 2020, "Laser Induced Phased Arrays (LIPA) to Detect Nested Features in Additively Manufactured Components," Mater. Des., **187**, p.108412.

[40] Fan, C., Caleap, M., Pan, M., and Drinkwater, B. W., 2014, "A Comparison Between Ultrasonic Array Beamforming and Super Resolution Imaging Algorithms for Non-destructive Evaluation," Ultrasonics, **54**(7), pp. 1842–1850.

[41] Holmes, C., Drinkwater, B. W., and Wilcox, P. D., 2005, "Post-processing of the Full Matrix of Ultrasonic Transmit–Receive Array Data for Non-destructive Evaluation," NDT E Int., **38**(8), pp. 701–711.

[42] COMSOL AB, 2018, COMSOL Multiphysics®. Stockholm, Sweden.